PHYSICAL REVIEW B VOLUME 41, NUMBER 9 15 MARCH 1990-II

Subband structure and plasmon-phonon coupled excitations in the accumulation layer of ZnO

Hong Yu and J. C. Hermanson
Department of Physics, Montana State University, Bozeman, Montana 59717

(Received 18 September 1989)

Calculations of electronic subbands and collective excitations are presented for strong accumulation layers in ZnO. Our model for this system is that of a free-electron gas with an effective mass embedded in a dielectric medium that supports lattice vibrations. Allowance is made for the conduction electrons to tunnel into the surface barrier. The effects of a position-dependent effective mass and of exchange and correlation are also considered. Using a nonlocal dielectric response formalism based on the random-phase approximation, we obtain the dispersion and line shapes of both intrasubband and intersubband plasmons. Evidence is found for two-dimensional intrasubband plasmons, as well as intersubband and "acoustic" plasmons; the latter have a nearly linear dispersion relation. When lattice vibrations are included, coupled plasmon-phonon modes or "plasmarons" are obtained. Some of these modes have been observed in earlier high-resolution electron-energy-loss spectroscopy experiments.

I. INTRODUCTION

Space-charge layers at semiconductor surfaces provide an excellent opportunity to study collective excitations of a nonuniform electron gas High-resolution electron-energy-loss spectroscopy (HREELS) (Refs. 1 and 2) is a particularly useful probe of these excitations because its effective sampling depth is on the order of the width of the space-charge region, namely 100 Å. Thus this technique is sensitive to the dispersion of plasmons on the same scale of wavelengths that characterizes the charge-density profile. Unfortunately, the limited angular resolution of most HREELS facilities does not permit the direct measurement of the frequency–wave-vector dispersion relations of the excitations. As a result, it is necessary to couple theoretical calculations of energy-loss spectra with the observations to elucidate the fundamental physics.

Until recently, theoretical studies of plasmons in space-charge layers have relied on a simplified picture in which the conduction electron response at a point in space depends only on the local electrical field.[31] However, typical screening lengths in these systems are on the order of 100 Å, and so nonlocal response is expected to play a crucial role. Ehlers and Mills[4] have presented a random-phase approximation (RPA) formalism for incorporating nonlocal effects in the inelastic scattering efficiency, and have reported calculations of plasmon dispersion and energy-loss spectra for depletion and accumulation layers on GaAs. The first step in this approach is the self-consistent determination of the energy levels and wave functions for a jellium-like model of the conduction electron system in the semiconductor. With these results in hand, one proceeds to solve the integral equation for the density response in the RPA; this response determines the plasmon spectrum. In a previous paper,[5] we reported nonlocal response calculations for accumulation layers on InAs, a system for which HREELS data were available for comparison. Our results included the dispersion, localization and line shapes of intersubband as well as intrasubband plasmons. We found evidence for two-dimensional (2D) and acoustic plasmons and studied the damping of all modes. When the phonon response was included, we obtained coupled plasmon-phonon modes or "plasmarons" which confirmed earlier interpretations of HREEL spectra[6] for InAs(110) exposed to atomic hydrogen.

In the present paper we present calculations of (1) the self-consistent electronic structure of the subbands and (2) the dynamical response of the electron-phonon system, for accumulation layers on ZnO. The latter system possesses a strongly localized electron gas[7] with a length scale of about 10 Å. One anticipates that such a system may exhibit 2D behavior[8] because a large majority of the conduction electrons inside in the lowest subband, whose spatial extent is much smaller than typical wavelengths involved in HREELS. Further, this material is of considerable interest because it stands at the ionic limit of the class of semiconducting solids. Finally, on account of the strong localization of the conduction electrons near the surface, the behavior of this system may be sensitive to microscopic details usually ignored in space-charge layers, such as tunneling into the surface barrier, position dependence of the effective mass, and exchange and correlation.[9]

Our paper is organized as follows. The self-consistent electronic subbands and wave functions are determined in the next section, for a simple model of the accumulation layer in ZnO. While the method for obtaining the electronic structure is closely related to that introduced by Ehlers and Mills[4] and applied by us to InAs accumulation layers,[5] we have extended it to allow us to consider the microscopic effects mentioned in the last paragraph. Section III summarizes our adaptation of the nonlocal response formalism[4] to our model system and contains a discussion of the various plasmon modes we obtained.

Phonon response is added in Sec. IV, and coupled plasmon-phonon modes are obtained. These modes are related to peaks observed in HREELS spectra of ZnO surfaces exposed to atomic hydrogen.[10–12] Section V contains our summary and conclusions.

II. SUBBAND ELECTRONIC STRUCTURE

In this section we summarize our physical model of the ZnO accumulation layer and the main features of the electronic structure associated with the subbands. The model is described as follows. A semiconducting slab of thickness $L-2z_0$, dielectric constant ϵ_∞, and effective mass m^* is centered between two infinite potential barriers at $z=0$ and $z=L$ chosen for computational convenience; see Fig. 1. Because the accumulation layer is localized within a few atomic layers near the surface, electron tunneling into the vacuum may play an important role.[13] To include the effects of tunneling we fill the two regions of width z_0 between the slab and the infinite barriers with potential barriers of height E_b equal to the electron affinity; i.e., the energy difference between the vacuum level and the conduction-band minimum. We choose z_0 sufficiently large compared with the decay length of the wave function that the shapes of the charge density and potential are independent of it. The conduction electrons inside the dielectric slab are treated as a free-electron gas characterized by an effective mass m^*. Immediately outside the slab surfaces we place infinitely thin sheets of charge of areal density n_s representing the positively charged layer induced by exposing the surface to atomic hydrogen. We introduce a position-dependent effective mass[14] $m^*(z)$ varying continuously between m^* deep inside the slab and m_e, the free-electron mass, in the vacuum. Specifically, $m^*(z)=m_e$ inside the finite barriers and m^* in the dielectric slab, except that in a thin layer of width a immediately outside the slab (see Fig. 1) an exponential interpolation is inserted to connect the inner and outer masses in a continuous manner.

As a result of the translation symmetry parallel to the surface, the envelope function for the conduction electron may be written as

$$\psi_{q_\parallel,i}(\mathbf{x}_\parallel,z)=\frac{1}{A^{1/2}}e^{i\mathbf{q}_\parallel\cdot\mathbf{x}_\parallel}\phi_i(z)\ , \tag{2.1}$$

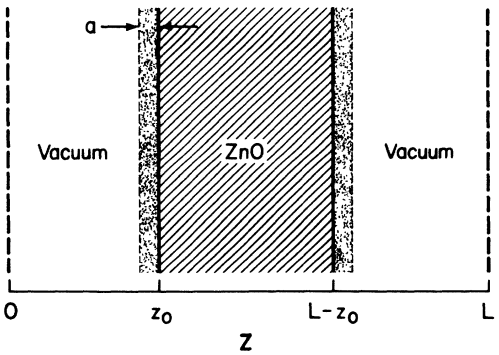

FIG. 1. Slab model of ZnO; see text for explanation.

where $\mathbf{x}_\parallel$ and $\mathbf{q}_\parallel$ are position and wave vector in the x-y plane, and A is the surface area of the slab; i is a quantum number for the motion in the z direction. The electronic energy can be written as

$$\varepsilon_i(\mathbf{q}_\parallel)=\frac{\hbar^2q_\parallel^2}{2m^*}+\varepsilon_i\ , \tag{2.2}$$

where ε_i denotes the energy minimum of the ith subband in the potential well caused by the accumulation layer, and we have assumed the transverse mass is m^*, independent of position. Given a position-dependent longitudinal mass as defined above, the wave functions $\phi_i(z)$ satisfy a one-dimensional Schrödinger equation of the BenDaniel-Duke form:[15]

$$-\frac{\hbar}{2}\frac{d}{dz}\left[\frac{1}{m^*(z)}\frac{d\phi_i(z)}{dz}\right]+V_{\text{eff}}(z)\phi_i(z)=\varepsilon_i\phi_i(z)\ . \tag{2.3}$$

In this equation, the effective potential is given by

$$V_{\text{eff}}(z)=V_B(z)+V_H(z)+V_{\text{xc}}(z)\ , \tag{2.4}$$

where $V_B(z)$ represents the potential barrier of height[16] $E_b=4.1$ eV. In Eq. (2.4), $V_H(z)$ is the Hartree potential of the conduction-electron system, and is related to the charge density by Poisson's equation

$$V_H(z)=-\frac{2\pi e^2}{\varepsilon_\infty}\int_0^L[n(z')-n_D(z')]|z-z'|dz'\ , \tag{2.5}$$

where $n_D(z)$ is the charge density of the ionized donors, given by the constant value n_+ inside the slab and zero outside. In the case of ZnO, n_+ is many orders of magnitude smaller than $n(z)$ in the accumulation region; in the calculations presented below, we assume n_+ vanishes. The boundary conditions

$$V_H(z=L/2)=0\ , \tag{2.6a}$$

$$\left.\frac{dV_H(z)}{dz}\right|_{z=z_0}-\left.\frac{dV_H(z)}{dz}\right|_{x=L-z_0}=-\frac{4\pi e^2}{\varepsilon_\infty}2n_s\ , \tag{2.6b}$$

ensure that we measure all energies from the bottom of the bulk conduction band. The free-carrier density at depth z is given at zero temperature by

$$n(z)=\frac{m^*}{\pi\hbar^2}\sum_i\theta(E_F-\varepsilon_i)(E_F-\varepsilon_i)|\phi_i(z)|^2 \tag{2.7}$$

with θ the unit step function, equal to unity (zero) for positive (negative) values of its argument, and E_F the Fermi energy, determined by the condition of charge neutrality,

$$n_{\text{tot}}=\frac{m^*}{\pi\hbar^2}\sum_i\theta(E_F-\varepsilon_i)(E_F-\varepsilon_i) \tag{2.8}$$

and n_{tot} is the areal electron density given by

$$n_{\text{tot}}=\int_0^L n(z)dz=n_+(L-2z_0)+2n_s\ . \tag{2.9}$$

In Eqs. (2.7) and (2.8), the sum over subband index i includes occupied states only and a constant effective mass was assumed. The generalization of Eq. (2.7) to finite temperatures is given in Ref. 4.

The exchange-correlation potential V_{xc} was adopted from the Hohenberg-Kohn-Sham local-density approximation;[17] we chose the simple analytic form of Hedin and Lundqvist:[18]

$$V_{\mathrm{xc}}(z)=-[1+0.7734\ln(1+x^{-1})]\frac{2}{\pi\alpha r_s}\ \mathrm{Ry}^* \tag{2.10}$$

with

$$\alpha=\left[\frac{4}{9\pi}\right]^{1/3},\quad x\equiv x(z)=\frac{r_s}{21},$$
$$r_s\equiv r_s(z)=[\tfrac{4}{3}\pi(a^*)^3n(z)]^{-1/3},$$
$$a^*=\frac{\varepsilon_\infty\hbar^2}{m^*e^2},\quad 1\ \mathrm{Ry}^*=\frac{e^2}{2\varepsilon_\infty a^*}. \tag{2.11}$$

As in our earlier work,[5] it is convenient to use a Fourier representation for the wave function. The wave functions were expanded in a sine series which vanishes at the walls $z=O,L$:

$$\phi_i(z)=\left[\frac{2}{L}\right]^{1/2}\sum_{j=1}^{\infty}b_{ij}\sin\left[j\frac{\pi z}{L}\right]. \tag{2.12}$$

With this expansion Eq. (2.3) is transformed into the matrix equation

$$\sum_{j'=1}^{\infty}M_{jj'}b_{ij'}=\varepsilon_i b_{ij},\quad i,j=1,2,\ldots. \tag{2.13}$$

An explicit form of the matrix $M_{jj'}$ is rather lengthy, and is given elsewhere.[14] As before in our work on GaAs (Ref. 2) and InAs,[5] we used a simple convergence-factor technique to achieve self-consistency between the charge density and potential.

In the calculations for ZnO, the parameters to be specified include n_s and n_+, the slab thickness $L-2z_0$, the number of sine waves N_{sine} kept in the expansion of $\phi_i(z)$, the width z_0 of the finite potential barrier, the width a of the interpolation region for the effective mass, and the dielectric constant and effective mass. The total thickness L was chosen large enough to simulate a semi-infinite geometry: $q_\parallel L \gg 1$, where $q_\parallel = 0.01$ Å is a typical surface wave-vector transfer in HREELS for ZnO. The optimum choice for N_{sine} depends on the slab thickness. The typical width of the accumulation layer is of order 10 Å; thus the smallest half wavelength in the sine expansion basis must be of this order, or $L/N_{\mathrm{sine}}\approx 10$. After careful examination we chose the values $L=500$ Å and $N_{\mathrm{sine}}=60$ to provide an accurate simulation of semi-infinite geometry.

The charge-density profile and self-consistent electron-electron potential ($V_{\mathrm{eff}}-V_B$) are shown in Fig. 2 for ZnO with $n_s=3\times10^{13}$ cm^{-2} and $n_+=0$. The solid lines show our results including exchange and correlation, while the dotted lines were obtained by neglecting these effects. The calculations shown in Fig. 2 included the effects of the surface barrier but assumed that the effective mass is independent of position: $L=500$ Å, $z_0=10$ Å, and $a=0$ Å. The present results are in good agreement with previous results[7] on the subband electronic structure of ZnO accumulation layers computed with a different method. We find that more than 90% of the conduction electrons occupy the lowest subband, the remainder occupying mainly the second subband. The charge density is localized within 8 Å of the surface plane because of the strong electric field evident in Fig. 2. Electrons in the first subband exhibit very little tunneling into the vacuum region; the electron density found outside the surface comes primarily from the second subband. Since the density essentially vanishes within 3 Å of the surface plane, our choice of surface barrier width, namely 10 Å, is adequate to ensure that the results do not depend on the boundary condition. Although exchange and correlation affect the charge density only slightly on the scale seen in Fig. 2, they do sharpen somewhat the electron density contributed by the first subband. The calculated charge density, including the effects of a position-dependent effective mass, is shown in Fig. 3 for two choices of the thickness a of the interpolation region. For comparison, the density obtained for constant m^* is indicated by the dashed line; the dotted line gives the result when tunneling is neglect-

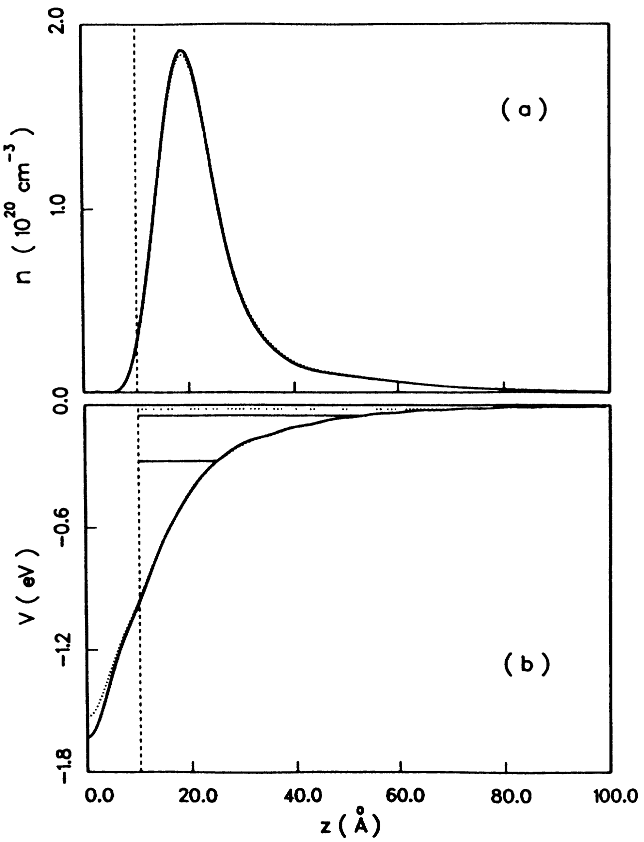

FIG. 2. (a) Self-consistent conduction-electron density and (b) electron-electron potential for ZnO accumulation layer with $n_s=3\times10^{13}$ cm^{-2}; other parameters are explained in the text. In both panels the results calculated with (without) exchange and correlation effects are given by solid (dotted) lines. The vertical dashed lines indicate the position of the surface plane.

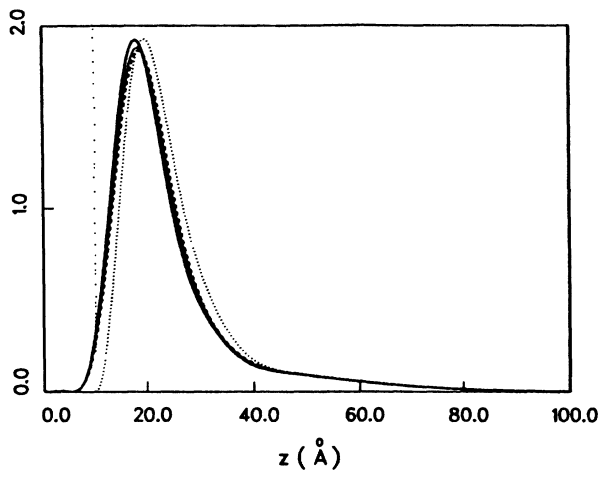

FIG. 3. Conduction-electron density for ZnO. Thick solid line: same as Fig. 1(a). Other results computed for $a = 10$ Å (thin solid line), constant m^* (dashed line), and $z_0 = 0$ (dotted line).

ed ($z_0 = 0$). A reasonable value for a is expected to be about 2 Å, or roughly the interplanar separation. Figure 3 shows that tunneling shifts the peak of the charge density 3 or 4 Å closer to the surface while keeping its shape almost unchanged.

Figure 4 shows the dependence of the subband energies and occupation numbers, and of the Fermi level and band bending, on the surface charge density and the temperature. To facilitate comparison with the results of Eger *et al.*[7] we have shifted the zero of energy to the surface potential, and we have included tunneling and exchange correlation as described above. Our room-temperature results, given in Fig. 4(a), are in excellent agreement with the earlier work.[7] At room temperature there are generally two subbands below E_F, and the interband separations and band bending increase with n_s as expected. Note the nearly linear behavior of the curves in Fig. 4(a) when $n_s > 4 \times 10^{13}$ cm^{-2}, and the smooth behavior of the occupation numbers there. Below $n_s = 2.5 \times 10^{13}$ cm^{-2}, only the first subband lies below the Fermi level. The dramatic changes of the occupation numbers at small n_s are associated with the passage from the 2D regime to the classical limit in which the thermal energy $k_B T$, or 26 meV, is larger than the subband separations. To explore the strict 2D limit we show results in Fig. 4(b) obtained at low temperature, $T = 10$ K. For $n_s > 3 \times 10^{13}$ cm^{-2} the energies of the lowest subbands agree closely with the room-temperature results, although above 6×10^{13} cm^{-2} three levels fall below E_F instead of the two found at 300 K. Also for low temperature, the occupation numbers vary monotonically with n_s. Indeed, when n_s is decreased below 10^{12} cm^{-2} the strict 2D limit is approached: essentially all of the conduction electrons are found in the lowest subband. The low-temperature calculations suggest that ZnO is well suited for studies of the 2D and quasi-2D electron gas. Finally, we note that because the 10- and 300-K results are so similar at and above 3×10^{13} cm^{-2}, a zero-temperature theory is expected to be adequate there.

III. DYNAMICS OF THE ELECTRON GAS

Having explored the subband electronic structure of ZnO accumulation layers in the last section, we turn our attention to the dynamical response of the system. Our approach is that of the nonlocal response formalism developed earlier within the random-phase approximation (RPA).[5] The energy-loss function in the dipole ap-

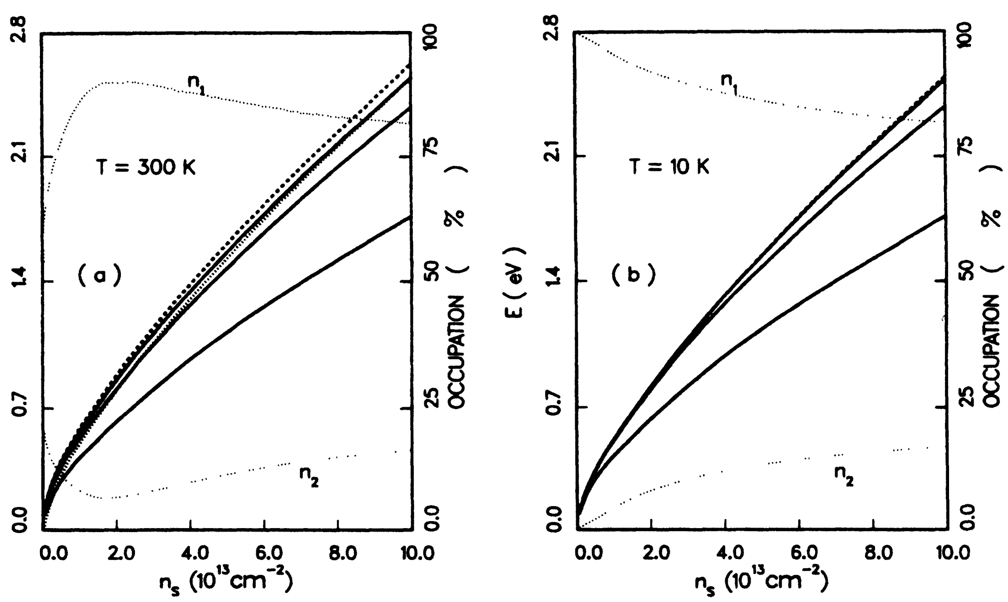

FIG. 4. Subband energy levels (solid lines) and occupation numbers (thin dotted lines) vs surface charge density for (a) $T = 300$ K and (b) $T = 10$ K. Also shown are the Fermi level (dashed lines) and band bending (thin dotted line). The zero of energy is the surface potential.

proximation is given at zero temperature by

$$P(q_{\parallel},\omega)=\frac{8e^2}{|1+\varepsilon|^2}\int_0^L dz\int_0^L dz'\,e^{-q_{\parallel}(z+z')}\times\mathrm{Im}[\chi(q_{\parallel},\omega;z,z')]\ , \tag{3.1}$$

where $q_{\parallel}$ and ω are the 2D wave vector and the frequency transferred to the electron gas by the scattered electron. The response function χ is related to the noninteracting response function χ_0 by the integral equation

$$\chi(q_{\parallel},\omega;z,z')=\chi_0(q_{\parallel},\omega;z,z')-\int_0^L dz_1\int_0^L dz_2\,\chi_0(q_{\parallel},\omega;z,z_1)V_e(q_{\parallel};z_1,z_2)\chi(q_{\parallel},\omega;z_2,z')\ , \tag{3.2}$$

where the interaction potential V_e contains the direct Coulomb interaction as well as exchange and correlation:

$$V_e(q_{\parallel};z_1,z_2)=\frac{2\pi e^2}{\varepsilon_\infty q_{\parallel}}\left\{e^{-q_{\parallel}|z_1-z_2|}+\frac{2}{\left[\left(\frac{\varepsilon_\infty+1}{\varepsilon_\infty-1}\right)^2 e^{2q_{\parallel}L}-1\right]}\left[\left(\frac{\varepsilon_\infty+1}{\varepsilon_\infty-1}\right)\cosh(z_1+z_2-L)+\cosh(z_1-z_2)\right]\right\}+\frac{dV_{\mathrm{xc}}(z)}{dn(z)}\delta(z_1-z_2)\ , \tag{3.3}$$

where $\delta(z_1-z_2)$ is the Dirac δ function. The bare response function χ_0 is defined at zero temperature by

$$\chi_0(q_{\parallel},\omega;z,z')=\sum_{\alpha,\alpha'}S_{\alpha\alpha'}(q_{\parallel},\omega)\phi_\alpha(z)\phi_\alpha(z')\times\phi_{\alpha'}(z)\phi_{\alpha'}(z')\ , \tag{3.4}$$

where the matrix $S_{\alpha\alpha'}$ is given by the 2D integral,

$$S_{\alpha\alpha'}(q_{\parallel},\omega)=2\int\frac{d^2k_{\parallel}f(E_{\mathbf{k}_{\parallel},\alpha})-f(E_{\mathbf{k}_{\parallel}+\mathbf{q}_{\parallel},\alpha'})}{(2\pi)^2E_{\mathbf{k}_{\parallel}+\mathbf{q}_{\parallel},\alpha'}-E_{\mathbf{k}_{\parallel},\alpha}+i\eta}\ ,\quad \eta\to 0^+\ . \tag{3.5}$$

In Eq. (3.5) the Fermi distribution function f at $T=0$ is

$$f(E)=\begin{cases}1, & E\le E_F\\ 0, & E>E_F\ .\end{cases} \tag{3.6}$$

Through contour integration[19] $S_{\alpha\alpha'}$ can be evaluated in closed form. The procedure for solving the integral equation for χ is formally identical to that used in our earlier work,[5] except that the matrix elements containing the exchange-correlation potential V_{xc} have to be evaluated numerically.

Figure 5 shows representative results for the energy-loss function when the phonon response is omitted. These results were obtained by solving Eq. (2.1) using the parameters assumed in Fig. 3 for several values of $q_{\parallel}$. A rather weak intrasubband plasmon peak due to the first subband is seen near $\omega=0.07$ eV for the smallest wave vector presented, $q_{\parallel}=0.001$ Å^{-1}. Also, a weak peak is seen near $\omega=0.025$ eV, associated with the interaction of surface plasmon modes on opposite faces of the slab; note that $q_{\parallel}L=0.5$. The transitions from the first subband to the second ($\omega\approx0.25$ eV), and from the first to the empty subband above the Fermi level ($\omega\approx0.3$ eV), can be identified by comparing the energy-level separations with the peak positions in Fig. 5. When $q_{\parallel}=0.006$ Å^{-1}, or $q_{\parallel}L=3$, the interaction of plasmon modes from opposite surfaces is weak, producing only a shoulder accompanying the main *intra*subband plasmon and a well-defined peak at $\omega\approx0.26$ eV due to an *inter*subband plasmon involving the first and second subbands. Further, a rather broad background due to single-particle (s.p.) excitations is found near the intersubband peak, and is attributed to transitions from the lowest subband.

The finite slab simulates a semi-infinite material when the wave vector is increased to $q_{\parallel}=0.01$ eV or $q_{\parallel}L=5$. Then the two intrasubband modes associated with the first band are degenerate, forming only one loss function peak as seen in Fig. 5. Since less than 10% of the conduction electrons occupy the second subband, the collective response of this band is anticipated to be weak and to have low energy. This intrasubband peak, strongly screened by the main plasmon,[5,20] can be seen at $\omega\approx0.08$ eV in Fig. 5. The broad feature below $\omega\approx0.2$ eV is attributed to s.p. excitations; this conclusion is supported by comparing the position of the dip near $\omega=0.18$ eV with the s.p. edge shown in Fig. 6. Note that the main plasmon gains in intensity as $q_{\parallel}$ is increased in Fig. 5, and that the mode is damped at large wave vectors $q_{\parallel}>0.1$ Å^{-1}, where it enters the s.p. continuum, into which it decays.

Figure 5 also presents the noninteracting (s.p.) spectra obtained by omitting the electron-electron interaction in Eq. (3.2). By energy-momentum conservation the excitation energy must fall in the ranges $(0,q_{\parallel}v_{F1})$, $(0,q_{\parallel}v_{F2})$, $(E_{12}-q_{\parallel}v_{F1},E_{12}+q_{\parallel}v_{F1})$ and peaks should be observed in the spectrum near the edges of these continua; v_{F1} and v_{F2} are the Fermi velocities of the first and second subbands. In our dispersion curves given below the two edges $E_{12}+q_{\parallel}v_{F1}$ and $q_{\parallel}v_{F1}$ are shown as dotted lines. The s.p. spectra at $q_{\parallel}=0.001$ Å^{-1} in Fig. 5 contain only one peak near the origin arising from the first subband, because of the near degeneracy of $q_{\parallel}v_{F1}$ and $q_{\parallel}v_{F2}$. The intersubband peak is seen near the interband energy separation $E_{12}=0.22$ eV. At $q_{\parallel}=0.06$ Å^{-1} there are two s.p. peaks at low energy and two intersubband transitions above 0.2 eV. For larger wave vectors the four peaks have larger energy separations. Note that, unlike the three-dimensional case, 2D intrasubband continua are peaked near their edges rather than displaying a triangle shape. Experimentally, only one intersubband transition and one intrasubband transition have been observed in Raman spectroscopy.[21]

We turn now to the dispersion relations of the plasmon modes portrayed in Fig. 5. By scanning the peak positions in these and other figures we mapped out the frequency versus wave-vector plots given in Fig. 6. Three modes are shown: intrasubband plasmons for the first and second subbands, and the intersubband mode involving transitions between these bands. We assign the lowest mode to an acoustic plasmon because of its nearly linear dispersion relation;[20,22] this mode may be described as an intrasubband plasmon in the second band that is screened by the plasmon in the first band. The middle mode in Fig. 6 (intrasubband plasmon arising from the lowest band) is closely approximated by the 2D frequency[8] ω_{2D} at small $q_{\parallel} < 0.02$ Å^{-1}, since the associated wavelength is much larger than the width of the density profile. The third mode in Fig. 6, an intersubband excitation, has a noticeable coupling with the middle mode even though its amplitude in the loss function is rather small. This coupling deforms the two associated dispersion curves so that the intrasubband mode is depressed below the 2D result; the intersubband mode follows the s.p. edge instead of crossing it.

The intersubband plasmon frequency $\omega_{12}(q_{\parallel} \rightarrow 0)$, 0.246 eV, is shifted upward from the transition energy E_{12},0.226 eV, because of the Coulomb interaction. This shift, which has been referred to as a "depolarization effect,"[23] can be estimated from the relation[5,8]

$$\tilde{\omega}_{12}(q_{\parallel} \rightarrow 0) = E_{12}(1+2\Delta_{12})^{1/2} , \qquad (3.7)$$

where $\Delta_{12} = n_s'^2 V_{1212}/E_{12}$ in terms of quantities defined earlier.[5] We obtained the values $V_{1212} = 7.01$ eV Å^2 and $\Delta_{12} = 0.084$. Thus, $\tilde{\omega}_{12} = 0.244$ eV, in good agreement with the value $\omega_{12} = 0.246$ eV found from the peak of the energy-loss function $P(q_{\parallel}, \omega)$.

The induced charge density[5,24] corresponding to $q_{\parallel} = 0.04$ Å^{-1} is presented in Fig. 7 as a function of frequency and depth below the surface. Notice the one-to-one correspondence between the peaks in this figure and the resonances shown in the top panel of Fig. 5. As mentioned above, the charge density of the second subband penetrates deeply into the surface; thus the weak induced

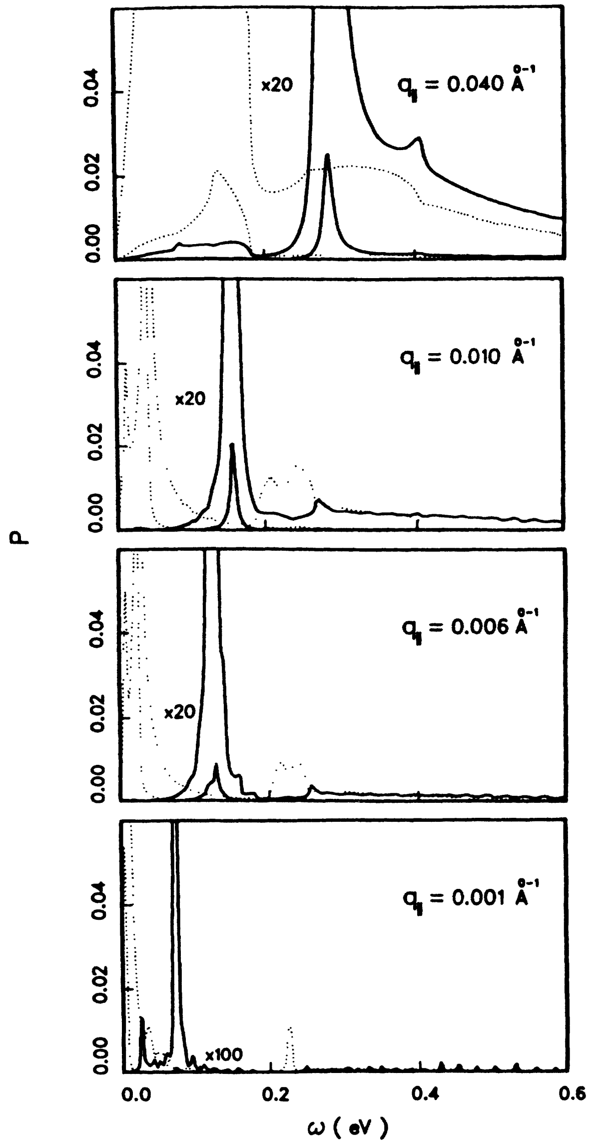

FIG. 5. Energy-loss function $P(q_{\parallel}, \omega)$ (solid lines) presented as a function of frequency for four values of the surface wave vector $q_{\parallel}$ in units of $2m^*e^2/\hbar^2$. The results obtained when the electron-electron interaction is omitted are shown by the dotted lines.

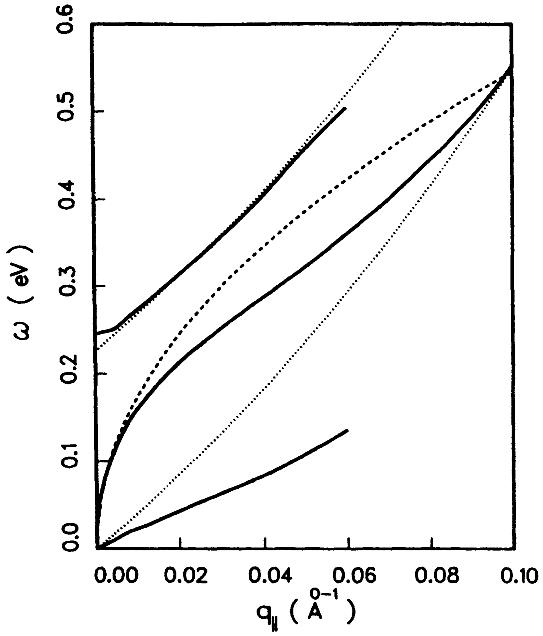

FIG. 6. Frequency–wave-vector dispersion curves (solid lines) for the plasmon peaks shown in Fig. 4. The dotted lines show the edges of the single-particle (s.p.) continua corresponding to intrasubband and intersubband excitation; ideal 2D dispersion is indicated by the dashed line.

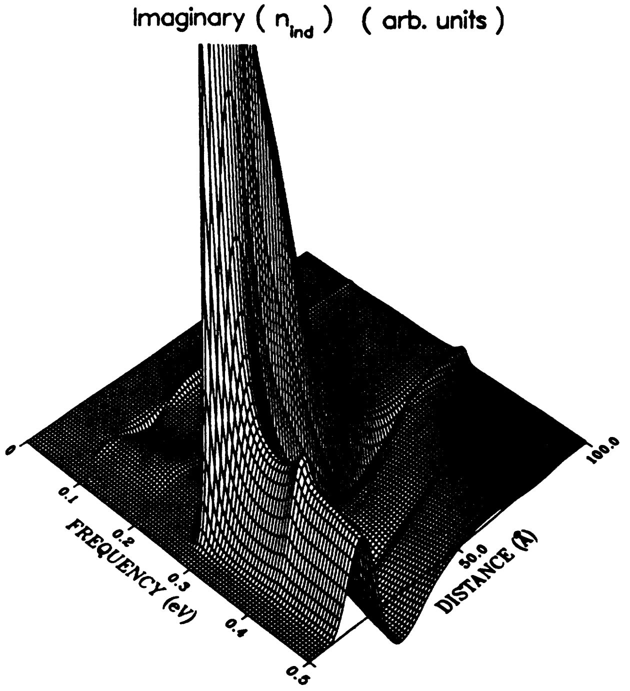

FIG. 7. Imaginary part of induced charge density shown as a function of frequency and distance below the surface for $q_{\parallel}=0.04$ Å^{-1}.

density near 0.09 eV in Fig. 7 supports the conclusion that the acoustic plasmon is a collective excitation of the second subband. The main peak near 0.28 eV is associated with the first subband. Interestingly, the shape of the main peak is similar to that of the charge density shown in Fig. 2, though the former is somewhat deeper inside the surface. Near the frequency of the intersubband plasmon, the induced charge density displays a surface localized peak.

IV. PLASMON-PHONON COUPLING

In order to compare our plasmon calculations with earlier theoretical and experimental[10-12] work we extend our model to include lattice vibrations as discussed in our previous calculations for InAs.[5] The dynamical lattice response is incorporated by replacing the static dielectric constant ε_∞ with a frequency-dependent dielectric constant given by

$$\epsilon(\omega)=\epsilon_\infty+\frac{\omega_{\mathrm{TO}}^2(\epsilon_0-\epsilon_\infty)}{\omega_{\mathrm{TO}}^2-\omega^2}\ , \tag{4.1}$$

where the long-wavelength transverse-optical phonon frequency ω_{TO} for ZnO is 0.0507 eV and the low- and high-frequency dielectric constants are[12] $\varepsilon_0=8.5$ and $\varepsilon_\infty=4$. A phenomenological phonon damping term $-i\omega\gamma$ was added in the denominator of Eq. (3.7), with $\gamma=0.003$ eV. When the phonon response is included in the dielectric function the plasmon and phonon modes may couple to form the so-called "plasmarons" denoted as ω_-, ω_0, and ω_+ modes.[10] The calculated dispersion curves are given in Fig. 8. These curves were obtained by monitoring the position of peaks in the energy loss function $P(q_{\parallel},\omega)$ as a function of wave vector. Though we do not present the individual loss functions, we will briefly discuss some aspects of them now. At the small wave vector $q_{\parallel}=0.005$ Å^{-1} there are four well-defined peaks at 0.05, 0.07, 0.14, and 0.26 eV, which are interpreted as the ω_-, ω_0, ω_+, and intersubband modes, respectively. As the wave vector is increased, the spectral weight of the ω_- mode is decreased, as expected; its frequency approaches the bulk

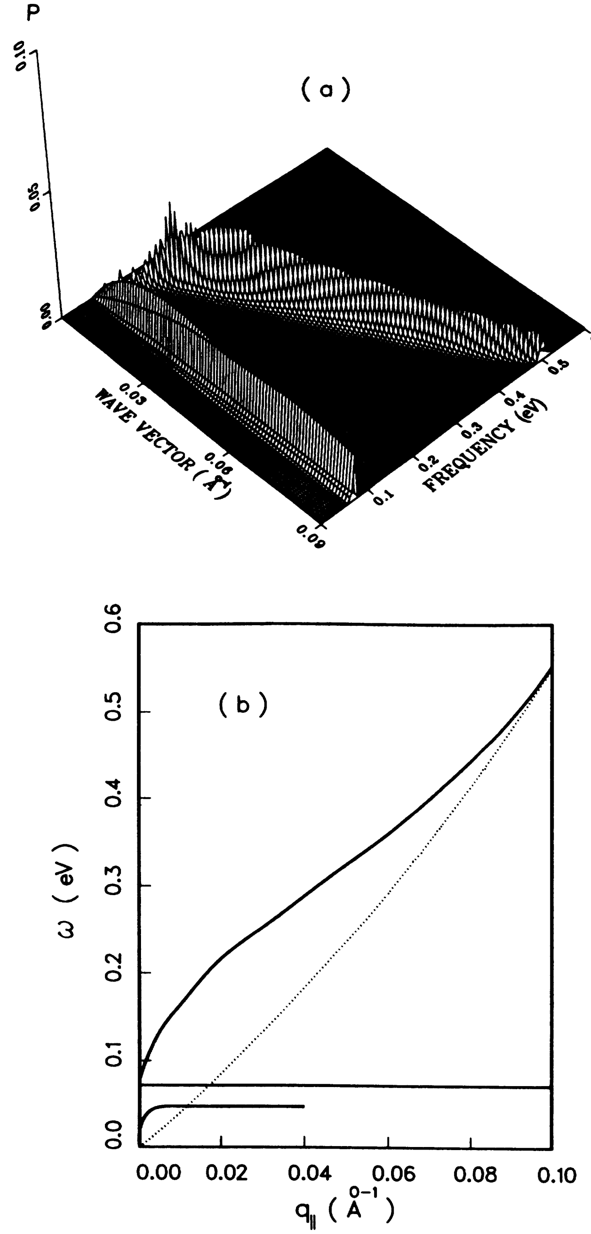

FIG. 8. (a) Energy-loss function $P(q_{\parallel},\omega)$ for surface charge density $n_s=3\times10^{13}$ cm^{-2}, including the effects of phonon response in units of $2m^*e^2/\hbar^2$. (b) Plasmaron dispersion curves obtained from (a); the intrasubband s.p. edge is shown by the dotted line.

phonon frequency and the mode becomes weak as $q_{\parallel}$ is increased. An intersubband s.p. background and an intrasubband s.p. edge are seen near 0.3 and 0.13 eV, respectively. The ω_0 surface phonon mode has an almost constant frequency but increases in intensity with increasing wave vector, while both the ω_+ and the intersubband modes are shifted upwards in frequency.

Figure 8 shows the energy-loss function $P(q_{\parallel},\omega)$ and the corresponding dispersion of the ω_-, ω_0, and ω_+ plasmarons but omits the acoustic and intersubband plasmons for greater clarity. Note that the lowest mode (ω_-) is very weak. The s.p. edges are seen as two dark lines in Fig. 8(a). The ω_+ mode interacts only weakly with the surface phonon mode denoted ω_0, largely because of the energy separation of these modes; the dispersion of the former mode is almost unchanged from Fig. 6. The ω_- plasmaron branch runs almost parallel to the ω_0 branch at large wave vectors. Our dispersion results are in reasonable agreement with earlier calculations[10,12] based on the strict 2D limit. There are some discrepancies at small wave vectors, where our ω_+ mode increases monotonically and the frequency of the ω_0 mode is nearly constant. Unlike InAs,[5] for the ZnO accumulation layer there is no evidence of phonon character for the ω_+ mode, and the ω_+ plasmaron disperses upward, not downward.

The energy-loss function and dispersion curves for a smaller surface charge density, $n_s = 1\times10^{12}$ cm^{-2}, are presented in Fig. 9. At this surface charge only the first subband is occupied. Here the ω_- mode is much stronger than in Fig. 8, because the intrasubband plasmon has lower frequency and therefore much stronger interaction with the phonon mode. The ω_+, on the other hand, is weaker, appearing as a shoulder on the loss peak attributed to the ω_0 mode. The dark lines represent the s.p. transitions from the occupied subband to higher subbands. Note that the ω_- mode is strongly Landau damped when it enters the s.p. region.

So far we have discussed the spectrum of collective excitations of the electron gas including the effects of phonon response by monitoring the peaks in the energy-loss function $P(q_{\parallel},\omega)$; the latter contains all information about the dynamical response of the medium. Now energy-loss spectrum $P(\omega)$, obtained from $P(q_{\parallel},\omega)$ by integrating over the wave vector, is a quantity that can be directly measured in HREELS. For small wave vectors these two functions are proportional.[25] The surface phonon on ZnO was first observed by Ibach.[26] He found that the relative intensity of the corresponding energy-loss peak became weaker with increasing impact energy. Noting that the probe depth is of order $q_{\parallel}^{-1} \sim E_1^{1/2}$, where E_1 is the impact energy, our results for the ω_0 peak intensity are consistent with the observed behavior:[26] the phonon peak decreases in intensity when the wave vector decreases. For large probe depths (small $q_{\parallel}$) the modes that extend deeper into the material are preferentially excited (intersubband mode, for example), while for small probe depths (large $q_{\parallel}$) the surface-localized modes (surface phonon and main intrasubband plasmon, for example) are dominant.

In order to make quantitative comparison with the data,[10,12] we carried out the wave-vector integration for $P(\omega)$ in the same way as in Ref. 5. We did not, however, convolve our spectra to simulate instrumental broadening. The resulting spectra are given in Fig. 10 for various impact energies E_0 and an angle of incidence of the primary electrons of 55°. The three plasmaron peaks are well separated, as noted earlier.[5] The lowest mode (ω_-) is sharp and has little dispersion; it evolves into a bulk phonon at large wave vector (small E_0). The spectral

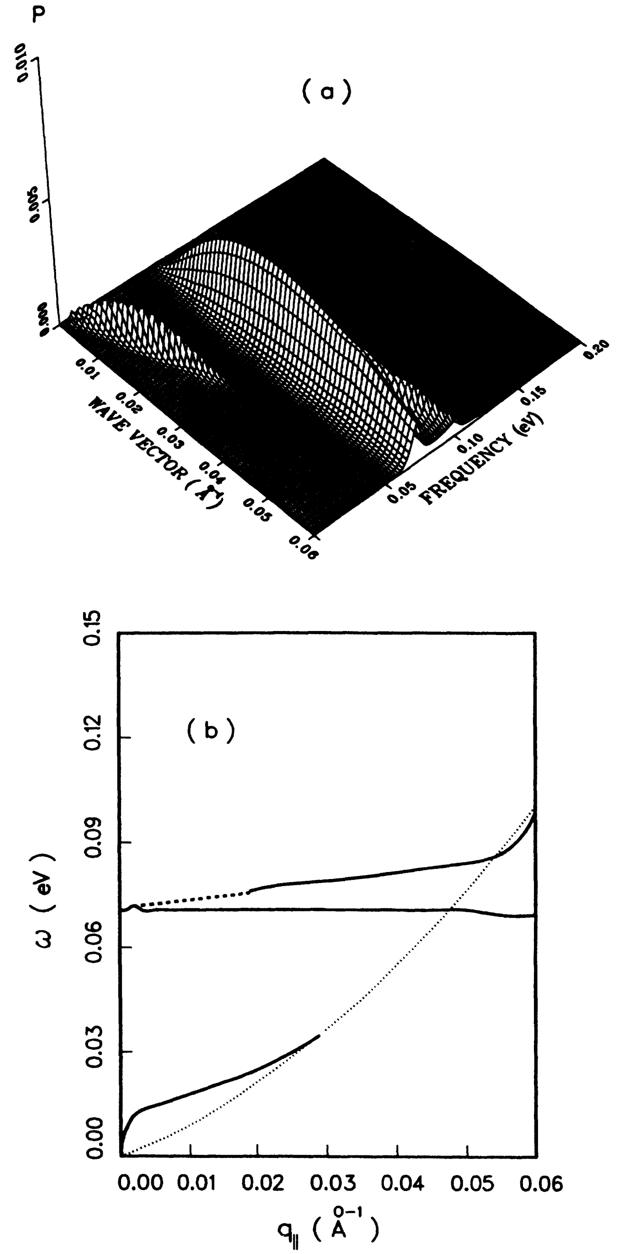

FIG. 9. (a) Energy-loss function for surface charge density $n_s = 1\times10^{12}$ cm^{-2} including the effects of phonon response. (b) Plasmaron dispersion curves obtained from (a); the intrasubband single-particle (s.p.) edge is shown by the dotted line.

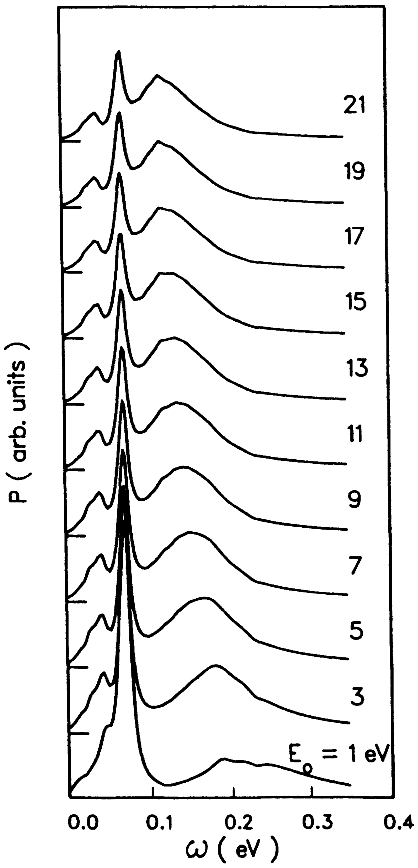

FIG. 10. Energy-loss spectrum $P(\omega)$ obtained by integrating $P(q_{\parallel},\omega)$ over $q_{\parallel}$, for various values of the impact energy E_0; $n_s = 3\times 10^{13}$ cm^{-2}.

weight of the surface phonon mode (ω_0) increases as the HREELS probe depth decreases. Further, the effects of the steep dispersion of the highest mode (ω_+) can be seen clearly in Fig. 10: as the impact energy decreases, the peak maximum moves to higher energy and the peak becomes broader. The s.p. excitations (intrasubband as well as intersubband) provide a noticeable background in the region of the ω_- and ω_+ peaks. Figure 10 also contains evidence for an intersubband plasmon. Because of its surface localization this mode is only seen at low impact energies. When E_0 is reduced to 3 eV a shoulder is visible on the high-frequency side of the ω_+ peak; the shoulder becomes a weak peak at a frequency of about 0.25 eV when the impact energy is 1 eV. The identification of this feature as an intersubband plasmon is suggested by noting that the intersubband transition energy is 0.24 eV. The intensity of the intersubband peak can be enhanced by increasing the angle of incidence (i.e., decreasing the probe depth), as shown by our calculations presented in Fig. 11. The peak gains significant strength as the angle of incidence increases from 20° to 60° at 1-eV impact energy.

Gersten *et al.*[12] performed HREELS experiments on the oxygen face of ZnO in the presence of adsorbed hydrogen which produced a strong accumulation layer. They observed the ω_0 and ω_+ modes only. On comparing their HREELS data (Fig. 4 of Ref. 12) with our calculated spectra given in Fig. 10, we note a similar behavior of the two peaks common to both figures. The frequency of our ω_+ mode is slightly lower than that of the experimental peak, suggesting that the surface charge we assumed, $n_s = 3\times 10^{13}$ cm^{-2}, is lower than the actual charge present in the experiment. Only the value of μn_s, where μ is the surface mobility, was quoted in the experiment.[12]

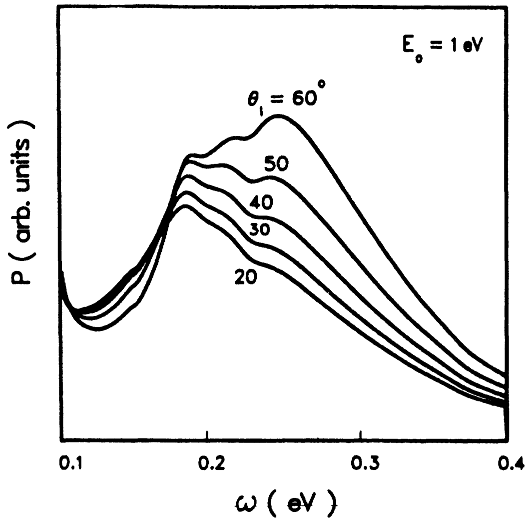

FIG. 11. Energy-loss spectrum at 1 eV impact energy for various angles of incidence θ_I of the primary electron beam; $n_s = 3\times 10^{13}$ cm^{-2}.

V. SUMMARY AND CONCLUSIONS

We determined the self-consistent electronic structure of strong accumulation layers on ZnO. The subband energy levels and wave functions were found to be only weakly affected by factors such as the position dependence of the effective mass, tunneling beneath the surface barrier, and exchange and correlation. Using a nonlocal description of dielectric response within the RPA, we applied our subband calculations to predict the collective excitations of the system. We obtained dispersion relations for both intersubband and intrasubband plasmons. By including a simple model of photon response, plasmaron dispersion was also studied. Beyond providing a physical picture of the excitations in the accumulation layer, we computed HREELS spectra for comparison with the data and calculations reported earlier.[10,12] Our results are in qualitative agreement with the observations. As yet, neither the ω_- plasmaron mode nor the intersubband plasmon has been observed in HREELS. Higher resolution may yield better understanding of these excitations. Also, experiments done at varying impact energies and angles of incidence would be useful in clarifying the localization properties of the modes.

ACKNOWLEDGMENTS

This work was supported by the National Science Foundation under Grant No. DMR-87-05879.

[1] R. Matz and H. Lüth, Phys. Rev. Lett. **46**, 500 (1981); A. Ritz and H. Lüth, *ibid.* **52**, 1242 (1984); A. Ritz and H. Lüth, J. Vac. Sci. Technol. B **3**, 1153 (1984); Z. J. Gray-Grychowski, R. A. Stradling, R. C. Egdell, P. J. Dobson, B. H. Joyce, and K. Woodbridge, Solid State Commun. **59**, 703 (1986); Surf. Sci. **186**, 482 (1987); M. G. Betti, U. del Pemino, and C. Mariani, Phys. Rev. B **39**, 5887 (1987).

[2] Y. Chen, S. Nannarone, J. Schäfer, J. C. Hermanson, and G. J. Lapeyre, Phys. Rev. B **39**, 7653 (1989).

[3] Ph. Panbin, J. P. Vigneron, and A. A. Lucas, Phys. Rev. B **32**, 8203 (1985).

[4] D. H. Ehlers and D. L. Mills, Phys. Rev. B **36**, 1051 (1987).

[5] Hong Yu and J. C. Hermanson, Phys. Rev. B **40**, 11 851 (1989).

[6] Y. Chen, J. C. Hermanson, and G. J. Lapeyre, Phys. Rev. B **39**, 12 682 (1989).

[7] D. Eger and Y. Goldstein, Phys. Rev. B **19**, 1089 (1979); D. Eger, A. Many, and Y. Goldstein, Surf. Sci. **58**, 18 (1976).

[8] F. Stern, Phys. Rev. Lett. **18**, 546 (1967).

[9] R. G. Dandrea, N. W. Ashcroft, and A. E. Carlsson, Phys. Rev. B **34**, 2097 (1986).

[10] A. Many, I. Wagner, J. I. Gersten, and Y. Goldstein, Phys. Rev. Lett. **46**, 1648 (1981).

[11] Y. Goldstein, A. Many and I. Wagner, Surf. Sci. **98**, 599 (1980); J. I. Gersten, *ibid.* **98**, 599 (1980); J. I. Gersten, *ibid.* **92**, 579 (1980); A. Puri and W. L. Schaich, Phys. Rev. B **31**, 974 (1985).

[12] J. I. Gersten, I. Wagner, A. Rosenthal, Y. Goldstein, A. Many, and R. E. Kirby, Phys. Rev. B **29**, 2458 (1984).

[13] F. Stern, Phys. Rev. B **5**, 489 (1972).

[14] Hong Yu, Ph. D. thesis, Montana State University.

[15] D. J. BenDaniel and C. B. Duke, Phys. Rev. **152**, 683 (1966).

[16] W. Göpel, J. Pollman, I. Ivanov, and B. Reihl, Phys. Rev. B **26**, 3144 (1982); I. Ivanov and J. Pollman, *ibid.* **24**, 7275 (1981); Solid State Commun. **36**, 361 (1980).

[17] P.Hoheberg and W. Kohn, Phys. Rev. **136**, B864 (1964); W. Kohn and L. J. Sham, *ibid.* **140**, A1133 (1965); L. J. Sham and W. Kohn, *ibid.* **145**, 561 (1966).

[18] L. Hedin and B. I. Lundqvist, J. Phys. C **4**, 2064 (1971).

[19] L. Wendler and R. Pechstedt, Phys. Status Solidi B **138**, 197 (1986).

[20] Y. Takada, J. Phys. Soc. Jpn. **43**, 1627 (1977).

[21] G. Fasol, N. Mestres, H. P. Hughes, A. Fisher, and K. Ploog, Phys. Rev. Lett. **56**, 1527 (1986); G. Fasol, N. Mestres, M. Dobers, A. Fisher, and K. Ploog, Phys. Rev. B **36**, 1565 (1987).

[22] S. Das Sarma and A. Madhukar, Phys. Rev. B **23**, 805 (1981); J. K. Jain and S. Das Sarma, *ibid.* **36**, 5949 (1987); G. E. Santoro and G. F. Guiliani, *ibid.* **37**, 937 (1988).

[23] D. A. Dahl and L. J. Sham, Phys. Rev. B **16**, 651 (1977).

[24] D. H. Ehlers, Phys. Rev. B **38**, 9706 (1988).

[25] H. Ibach and D. L. Mills, *Electron-Energy Loss Spectroscopy and Surface Vibration* (Academic, San Francisco, 1982).

[26] H. Ibach, Phys. Rev. Lett. **24**, 1416 (1970).

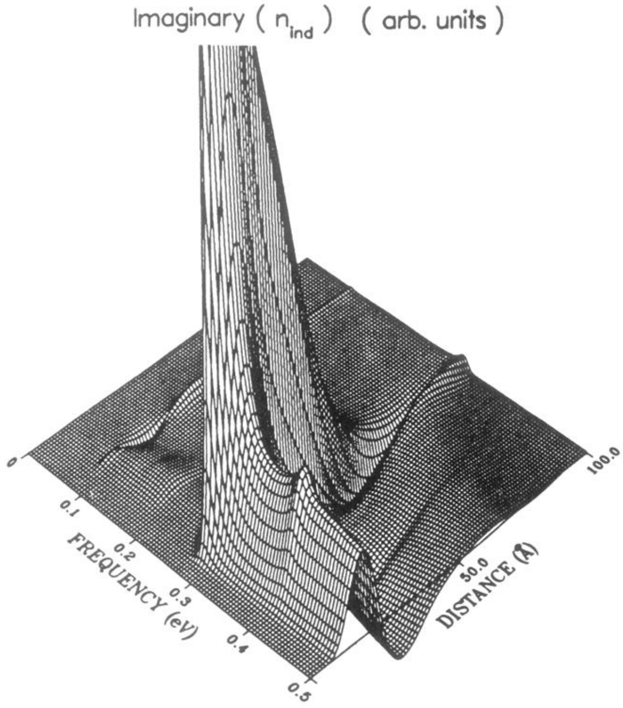

FIG. 7. Imaginary part of induced charge density shown as a function of frequency and distance below the surface for $q_{\|} = 0.04$ Å^{-1}.

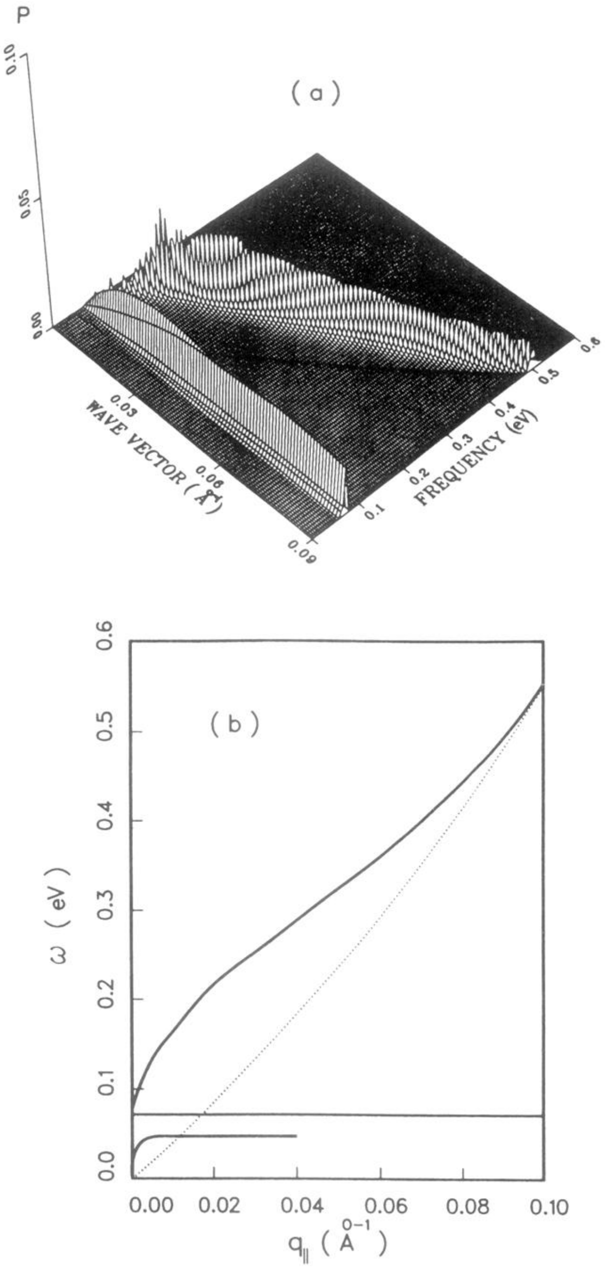

FIG. 8. (a) Energy-loss function $P(q_{\parallel},\omega)$ for surface charge density $n_s=3\times10^{13}$ cm^{-2}, including the effects of phonon response in units of $2m^*e^2/\hbar^2$. (b) Plasmaron dispersion curves obtained from (a); the intrasubband s.p. edge is shown by the dotted line.

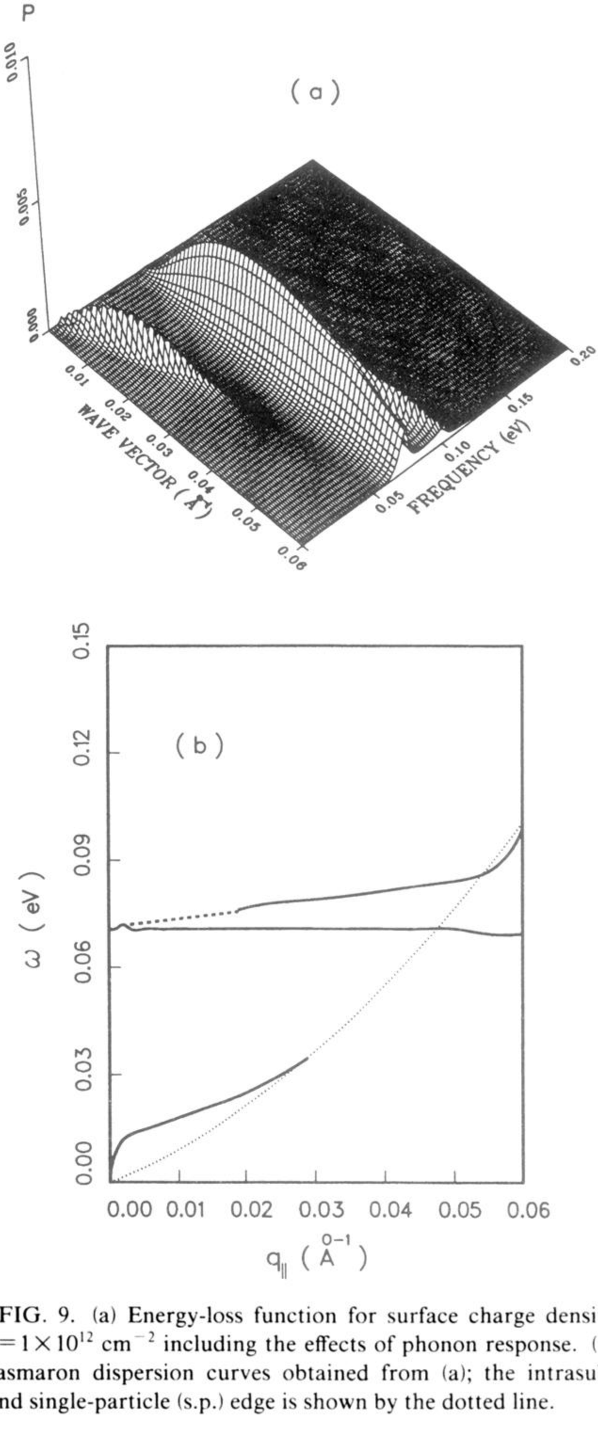

FIG. 9. (a) Energy-loss function for surface charge density $n_s=1\times10^{12}$ cm^{-2} including the effects of phonon response. (b) Plasmaron dispersion curves obtained from (a); the intrasubband single-particle (s.p.) edge is shown by the dotted line.